Dispersion of an Elevated Release in a Coastal Region

HAO JIN AND SETHU RAMAN

Department of Marine, Earth and Atmospheric Sciences, North Carolina State University, Raleigh, North Carolina

(Manuscript received 3 April 1995, in final form 8 December 1995)

ABSTRACT

This paper presents a study on air pollutant dispersion from an elevated accidental release from the space shuttle tower at the Kennedy Space Center in Florida under the influence of a stratified onshore flow. The temperature difference between land and ocean can generate a local sea–land circulation and a thermal internal boundary layer. Both play a significant role in the coastal dispersion. Results from a Gaussian dispersion model and those from numerical simulations show that the concentrations obtained from these two distinctly different methods are of the same order of magnitude and have similar patterns. Numerical simulations were performed by combining the Advanced Regional Prediction System with an Eulerian pollutant dispersion model. Numerical sensitivity experiments were conducted to investigate the effects of upwind stability, coastal topography, and calm wind condition. Numerical results also show that the dispersion pattern from a continuous release is significantly different from that of a finite release.

1. Introduction

Many cities and about half of the population around the world are located in economically active coastal regions; hence coastal regions are potential locations for the release of hazardous materials. Topography in coastal regions is generally quite complicated. The temperature difference between ocean and land can generate a local sea–land breeze circulation, and if rivers and cities are located in the coastal area, they can produce complex local thermal circulations. The surface temperature contrast between ocean and land initiates a thermal internal boundary layer (TIBL), which has a critical effect on shoreline dispersion.

In this paper, dispersion from the launch tower at the Kennedy Space Center (KSC) in Florida (28.5°N, 80.5°W) due to an accidental release is considered. The space shuttle launch pads are located at about 0.5 km inland of the Cape Canaveral coastline. The release is assumed to happen at the top of the 60-m launch tower with a strength of 9.887×10^{11} μg s^{-1} for a space shuttle. The pollutant release from the explosion of the space shuttle is considered as an elevated continuous point source. Coastal dispersion is evaluated using a Gaussian analytical dispersion model and an Eulerian dispersion model coupled with a mesoscale meteorological model.

The simulation domain is 40 km $\times$ 40 km with a horizontal resolution of 1 km $\times$ 1 km. KSC is located near the center of the simulation domain and is about 25 km from the western boundary and 20 km from the southern boundary (Fig. 1). The 6-km-wide Indian River is located to the west of the KSC, about 12 km away. The release is assumed to occur in the late morning as the land surface is warming up. The air temperature immediately above the ocean is assumed to be 295 K, about 6 K lower than that over land. Air temperature over the Indian River is assumed to be 297 K. Easterly onshore flow is stable with a speed of 6.5 m s^{-1}. These values are consistent with the general flow pattern over the region (Boybeyi and Raman 1992). Chemical reactions and decays of the pollutants are not taken into account. The effects of the plume buoyancy and dry and wet depositions are neglected. The dispersion is mostly affected by flow advection and turbulence diffusion processes.

The shoreline fumigation was studied by Deardorff and Willis (1982), Misra (1980), van Dop et al. (1979), and Venkatram (1988) using extended Gaussian models. These models illustrate a general method of dealing with dispersion in which the boundary layer undergoes a transition in properties. Yamada et al. (1992) used a 3D hydrodynamic atmospheric model and a random puff dispersion model to forecast the dispersion of airborne material along the California coast. A mesoscale modeling system (Uliasz 1993), which included a 3D mesoscale model with a Lagrangian particle model and an Eulerian grid model, was developed to investigate atmospheric flow and pollution dispersion over complex terrain. In general, Gaussian models are more suitable for smaller spatial scales. Mesoscale models that are coupled with dispersion models mentioned

Corresponding author address: Dr. Sethu Raman, Professor of Meteorology, Box 8208, Dept. of Marine, Earth and Atmospheric Sciences, Raleigh, NC 27695-8208.

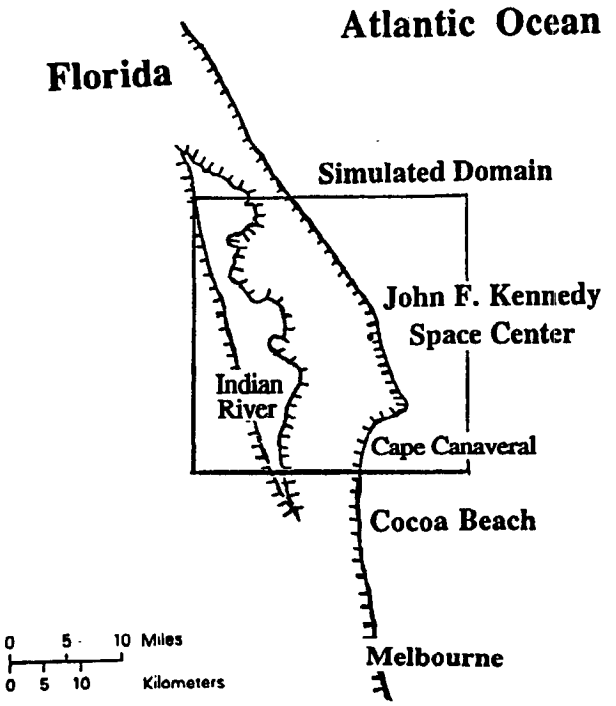

FIG. 1. Simulation domain (40 km × 40 km) along the Florida coastline with the Kennedy Space Center (KSC) located near the center.

above are often hydrostatic and are good for long range dispersion. So far, there have not been careful comparisons of results using Gaussian models and mesoscale dispersion models. A high-resolution, nonhydrostatic mesoscale model is required to couple with Eulerian dispersion model to study coastal dispersion.

An objective of this study is to compare the dispersion in a coastal region using two distinctly different models: a Gaussian model and an Eulerian model. The Gaussian dispersion model for the coastal region is discussed in section 2. Section 3 presents the numerical simulations using the Advanced Regional Prediction System (ARPS), a nonhydrostatic mesoscale meteorological model originally developed by the Center for Analysis and Prediction of Storms (CAPS), combined with an Eulerian pollutant dispersion model. Numerical sensitivity experiments are conducted to show the effects of upwind stability, release time, coastal topography, and calm wind condition.

2. Gaussian dispersion in the coastal region

Gaussian models are widely used in air quality studies. They are simple and easy to use, but have many limitations. A Gaussian model can be developed from a pollutant mass conservation equation as below:

$$\frac{\partial c}{\partial t} = -\left(u\frac{\partial c}{\partial x} + v\frac{\partial c}{\partial y} + w\frac{\partial c}{\partial z}\right) + \frac{\partial}{\partial x}\left(Kx\frac{\partial c}{\partial x}\right) + \frac{\partial}{\partial y}\left(Ky\frac{\partial c}{\partial y}\right) + \frac{\partial}{\partial z}\left(Kz\frac{\partial c}{\partial z}\right), \quad (1)$$

where c is pollutant concentration; u, v, and w are velocities in x, y, and z directions, respectively; and K_x, K_y, and K_z are the turbulence diffusion coefficients in x, y, and z directions, respectively. To get a Gaussian solution from the pollutant mass conservation equation, the following assumptions are generally made (Turner 1994): (i) emission from the source is continuous and constant; (ii) mass of the pollutant is conserved during the transport of pollutant—in other words, none of the material is removed or lost through chemical reaction, gravitational settling, or turbulent impact; and (iii) meteorological condition is steady state. The third assumption is not valid under light wind conditions and at great transport distance. Using the slender-plume approximation, that is, the diffusion in the mean wind direction is much less than mean wind advection, Eq. (1) can be simplified when the x direction is along the mean wind:

$$u\frac{\partial c}{\partial x} = K_y\frac{\partial^2 c}{\partial y^2} + Kz\frac{\partial^2 c}{\partial z^2}. \quad (2)$$

Gaussian models do not contain the pollutant source strength in the mass conservation equation. The source strength is usually obtained from the constant mass flux transported by mean wind; that is,

$$\iint ucdydz = Q_s, \quad (3)$$

where Q_s is the mass of the pollutant released per second.

Under the assumption of constant eddy diffusivity and uniform wind in vertical and horizontal directions, a Gaussian distribution is obtained. Thus, the Gaussian solutions are for use in simple meteorological background without wind shear. Theoretically, they are unsuitable for complex terrain. In real situations, homogenous wind and terrain are usually not present, especially in cities and coastal regions where most of the pollutants are generated and where local "urban heat island" circulations and sea–land breeze circulations dominate. However, modified Gaussian models are still used for air quality evaluations in cities and coastal regions. Effect of the TIBL is generally considered when Gaussian models are applied to shoreline dispersion (Misra 1980); however, local sea–land breeze circulations have not been included.

a. TIBL height

Dynamics of the TIBL is an important consideration to predict the dispersion in coastal regions. When a

stratified onshore flow occurs over a heated land surface, a mixed layer (or convective TIBL) forms and its depth increases with distance downwind of the shoreline. Venkatram (1988) derived the TIBL height based on thermal energy balance as

$$h^2(x) = h^2(0) + \frac{2}{\gamma(1-2F)U}\int_0^x \overline{w\theta_0}(x)dx, \quad (4)$$

where h is TIBL height (m), U the mean wind speed downwind, γ the potential temperature gradient over water, and F an entrainment fraction. If $\overline{w\theta_0}$ is constant, Eq. (4) can be reduced to the equations suggested by Weisman (1976) and Plate (1971) with different values of F. The value of F here is set as $1/7$, then the inversion heat flux is one-fifth of the surface flux. The TIBL height is not sensitive to the value F (Venkatram 1988). Because the surface heat flux $\overline{w\theta_0}$ is driven by temperature differential between the heated land and onshore flow, it is reasonable to assume

$$\overline{w\theta_0} = Au_*(\theta_L - \theta_W), \quad (5)$$

where the empirical factor A is likely to be site specific, u_* the downwind surface frictional velocity, θ_L the downwind land surface potential temperature, θ_W the upwind potential temperature over water, and γ the upwind vertical potential temperature gradient. For further simplification, assuming $h(0)$ equals zero, Venkatram (1977) suggested a relation as follows:

$$h = \frac{u_*}{U}\left[\frac{2(\theta_L - \theta_W)x}{\gamma(1-2F)}\right]^{1/2}, \quad (6)$$

where x is the downwind distance from the coastline. This equation is similar to the empirical one suggested by Raynor et al. (1975). Equation (6) indicates that the square of the TIBL height is proportional to the potential temperature difference between the land and the water, and is inversely proportional to the upwind vertical potential temperature gradient. The stronger the stability upwind, the shallower the TIBL. One problem is that Eq. (6) has singularity as $\gamma \to 0$ in the near-neutral condition and the TIBL height may be overestimated.

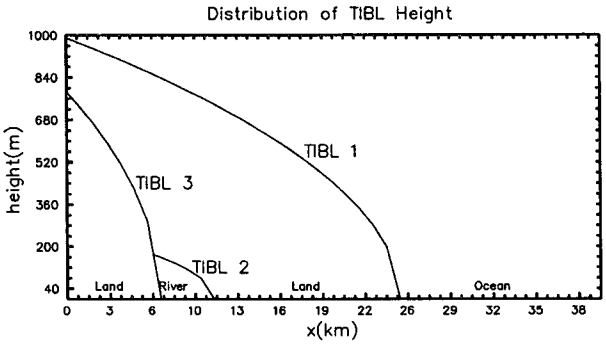

FIG. 2. Distribution of TIBL heights in a region with ocean–land–river–land interfaces.

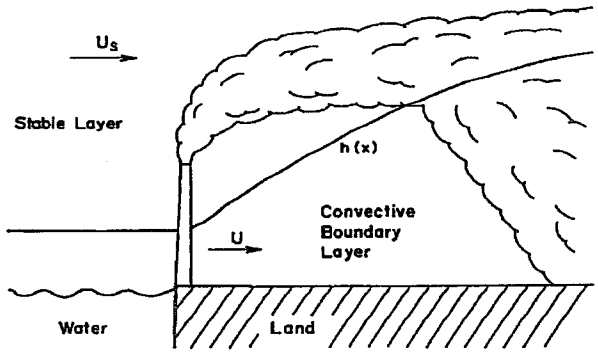

FIG. 3. Schematic of shoreline fumigation.

For this study the surface friction velocity u_* is obtained using the similarity theory in the boundary layer. The surface roughness over land is assumed to be 0.01 m. Roughness over the ocean is assumed as $0.035u_*^2/g$. The stability γ depends on the stability of upstream flow. When the Brunt–Väisälä frequency of inflow is 0.01 s^{-1}, the stability γ is about 0.003 K m^{-1} for the ocean, -0.003 K m^{-1} for the river surface, and 0.001 K m^{-1} for the land surface.

The structure of three TIBLs estimated by Eq. (6) is shown in Fig. 2. TIBL 1 caused by the temperature difference between ocean and land is the most important. The height of TIBL 1 can reach to about 600 m at 10 km from the coastline. This TIBL is unstable and affects a broad area of simulation domain. Above TIBL 1, the atmosphere is still very stable and controlled by the upstream inflow from the ocean. TIBL 2 that forms on the Indian River, is stable and very shallow (less than 200 m) because the Indian River is narrow and its temperature is cooler than the air above. The downwind part of the stable TIBL 2 above the land is destroyed by a convective TIBL 3 generated at the land–river boundary. Because of the low γ (less stable) over the Indian River, the height of TIBL 3 increases faster than that of TIBL 1. The air in the unstable TIBL 3 will mix with air in TIBL 1. This type of TIBL within a TIBL pattern can also be seen in numerical simulations in section 3b.

b. Gaussian dispersion

The TIBL caused by the temperature difference between ocean and land plays a very important role in the coastal fumigation. However, the local sea–land breeze circulation cannot be included since the Gaussian model is derived for a homogeneous wind condition. Figure 3 shows a schematic of shoreline fumigation. Usually the plume is initially embedded in the stable onshore flow. Fumigation is associated with the entrainment of the plume from the stable layer into the

growing TIBL. Within the TIBL, the atmosphere is unstable and the pollutant is assumed to be fully mixed in the vertical. Misra (1980) and van Dop et al. (1979) obtained the following equation using slightly different derivations:

$$c(x, y, 0) = \frac{Q_s}{2\pi h(x)} \int_0^x \frac{1}{\sigma_{ye} U} \times \exp\left(-\frac{p^2}{2}\right) \frac{dp}{dx'} \exp\left(-\frac{y^2}{2\sigma_{ye}^2}\right) dx', \quad (7)$$

where

$$p(x') = \frac{h(x') - h_e(x')}{\sigma_{zs}(x')} \quad (8)$$

and

$$\sigma_{ye}^2 = \sigma_{ys}^2(x') + \sigma_y^2(x, x'), \quad (9)$$

where Q_s is the strength of a continuous point source, $h(x)$ the height of the TIBL, $h_e(x)$ the effective height of point source, U the wind speed, and σ_{ys} and σ_{zs} are the lateral and vertical diffusions in the stable layer. Van Dop et al. (1979) assumed that plume spread in the TIBL is related to particle release at $x = 0$. This indicates

$$\sigma_y^2(x, x') = \sigma_y^2(x) - \sigma_y^2(x'). \quad (10)$$

Venkatram (1988) made an assumption that the rate of growth of σ_y in the TIBL will not be affected by convective turbulence and hence reduced Eq. (7) to a simpler form:

$$c(x, y, 0) = \frac{Q_s}{2\sqrt{2\pi} U \sigma_y h(x)} \left\{1 + \text{erf}\left[\frac{h(x) - h_e(x)}{\sqrt{2}\sigma_{zs}}\right]\right\} \times \exp\left(-\frac{y^2}{2\sigma_y^2}\right). \quad (11)$$

This may cause overestimation of the concentration distribution because the σ_y in the stable condition is smaller than that in the unstable condition. When the elevated point source is quite near the TIBL, it is preferable to use $\sigma_{\dot{y}}$ value in the convective TIBL.

Above the TIBL, atmosphere is still very stable and the dispersion there is not affected by the interface refractivity effects since the entrainment occurs at the top of the TIBL. Thus, the dispersion above the TIBL satisfies

$$c(x, y, z) = \frac{Q_s}{2\pi U \sigma_y \sigma_z} \times \exp\left(-\frac{y^2}{2\sigma_y^2}\right) \exp\left[-\frac{(z - h_e)^2}{2\sigma_z^2}\right]. \quad (12)$$

The stability classification system of the diffusion coefficients proposed by Pasquill and later modified by Gifford (known as the PG system) is the most popular one in air quality evaluation that defines six classes. Since the stability over the ocean is related to the temperature difference between surface water and air mass advected over it, it is not closely related to the local radiation inputs which is used in the PG system. The Pasquill–Gifford classification cannot characterize dispersion over water although the PG system works well over land where the diurnal radiative forcing plays a major role. To make use of the modified PG system for the open country by Briggs (1973), it is assumed that B class is over land and F class is over the ocean when the large-scale inflow with a speed of 6.5 m s^{-1} and a Brunt–Väisälä frequency of 0.01 s^{-1} passes over the heated land.

When the Gaussian dispersion is applied to the accidental release at KSC with a grid resolution of 1 km $\times$ 1 km in the horizontal and 25 m in the vertical, only TIBL 1 near the coastline is considered. The TIBLs caused by the existence of the Indian River are not important since the Indian River is too narrow and too far (12 km) from the release source. Using the coastal fumigation relation Eq. (11) and the stable dispersion relation equation (12), the pollutants are dispersed and transported in the downwind direction (Fig. 4). The horizontal extent of the plume (characterized by 2 $\times$ 10^4 μg m^{-3} contour) is about 5 km wide, and the maximum ground-level concentration is 3.925 $\times$ 10^6 μg m^{-3} located near the elevated source (Fig. 4a). From a vertical section of the concentration distribution through the continuous point source, it is obvious that the pollutant distribution is uniform in the vertical except at the top of TIBL 1 (Fig. 4b). Only few pollutants are transported above TIBL 1, and the distribution of the pollutants corresponds to be the shape of TIBL 1.

The sensitivity experiments show that the results from the Gaussian model are sensitive to the wind direction. If the plume central line is not parallel to the wind direction, the maximum concentration becomes much smaller. In the real atmosphere, wind is usually not in steady state, and it is difficult to detect the peak of the pollutants. Since the concentration decays exponentially with distance in the Gaussian distribution, the grid resolution and the position of the source affect the concentration in the whole domain. Many assumptions made in Gaussian dispersions impose limitations on their applicability. For example, the assumptions of complete mixing in the TIBL and the neglect of the local sea–land circulations do not reflect the real dynamics and thermodynamics. Numerical simulations may give more realistic solutions.

3. Numerical simulations

Three-dimensional numerical simulations in the coastal region are performed using the ARPS model

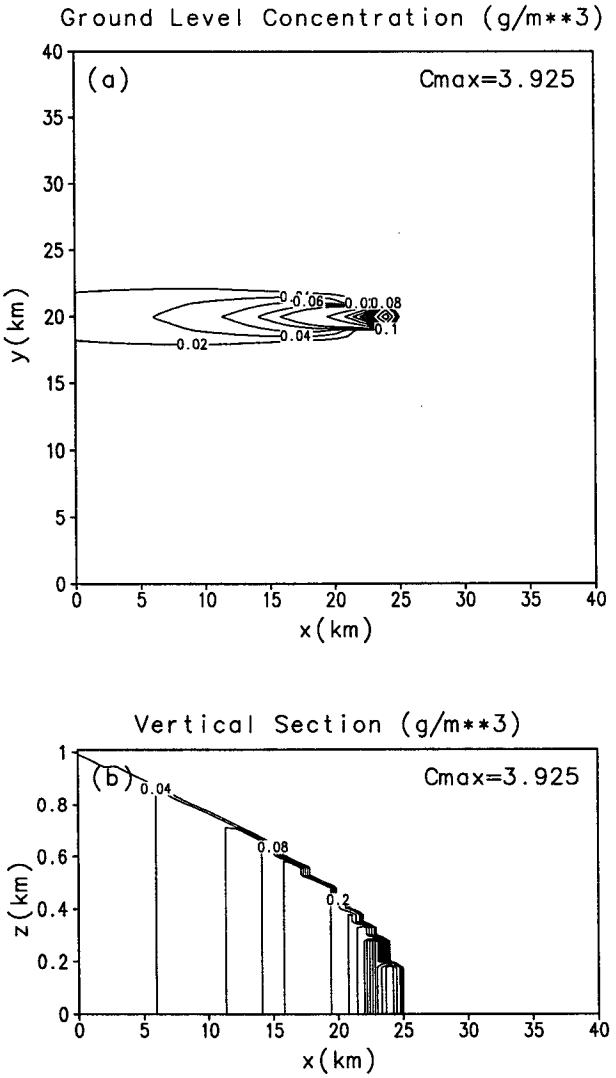

FIG. 4. Dispersion in the coastal region: (a) ground-level concentration (g m^{-3}) and (b) vertical section through the continuous point source at $y = 20$ km. The maximum ground level concentration is 3.925 g m^{-3}.

coupled with an Eulerian dispersion model. In addition to the TIBL effects, which are discussed in the previous Gaussian dispersion, the orientation of the coastline and shape of the Indian River, and its associated local circulations, are important factors included. The ARPS model and the initial conditions used in the model are briefly described in section 3a. Section 3b shows the comparison between numerical simulations and the Gaussian dispersion. The numerical sensitivity experiments are discussed in section 3c.

a. A brief description of the ARPS model

The ARPS model is a three-dimensional, nonhydrostatic and fully compressible primitive equations model (CAPS 1993). The simplified equations in a Cartesian coordinate system are given below. A pollutant conservation equation for concentration is added to predict the concentrations for this study. The equations are

$$\frac{\partial u}{\partial t} = -\left(u\frac{\partial u}{\partial x} + v\frac{\partial u}{\partial y} + w\frac{\partial u}{\partial z}\right) - \frac{1}{\rho}\frac{\partial(\bar{p} + p')}{\partial x} + fv + D_u, \quad (13)$$

$$\frac{\partial v}{\partial t} = -\left(u\frac{\partial v}{\partial x} + v\frac{\partial v}{\partial y} + w\frac{\partial v}{\partial z}\right) - \frac{1}{\rho}\frac{\partial(\bar{p} + p')}{\partial y} - fu + D_v, \quad (14)$$

$$\frac{\partial w}{\partial t} = -\left(u\frac{\partial w}{\partial x} + v\frac{\partial w}{\partial y} + w\frac{\partial w}{\partial z}\right) - \frac{1}{\rho}\frac{\partial(\bar{p} + p')}{\partial z} - g + D_w, \quad (15)$$

$$\frac{\partial \theta}{\partial t} = -\left(u\frac{\partial \theta}{\partial x} + v\frac{\partial \theta}{\partial y} + w\frac{\partial \theta}{\partial z}\right) + D_\theta, \quad (16)$$

$$\frac{\partial p'}{\partial t} = -\left(u\frac{\partial p'}{\partial x} + v\frac{\partial p'}{\partial y} + w\frac{\partial p'}{\partial z}\right) - \left(u\frac{\partial \bar{p}}{\partial x} + v\frac{\partial \bar{p}}{\partial y} + w\frac{\partial \bar{p}}{\partial z}\right) - \rho c_s^2\left(\frac{\partial u}{\partial x} + \frac{\partial v}{\partial y} + \frac{\partial w}{\partial z}\right), \quad (17)$$

$$\frac{\partial c}{\partial t} = -\left(u\frac{\partial c}{\partial x} + v\frac{\partial c}{\partial y} + w\frac{\partial c}{\partial z}\right) + D_c + S_c, \quad (18)$$

where u, v, and w are the Cartesian components of velocity; θ the potential temperature; $\bar{p}$ the base-state pressure; p' the pressure perturbation; ρ the density; c the air pollutant; f the Coriolis parameter; c_s the speed of sound; and S_c the source of pollutants. Terms D_u, D_v, and D_w indicate the subgrid-scale turbulence mixing terms in the u, v, and w momentum equations, while D_θ and D_c are mixing terms in the potential temperature and the air pollutant equations. These terms are expressed in terms of Reynolds stress terms τ_{ij}:

$$D_u = \frac{\partial \tau_{11}}{\partial x} + \frac{\partial \tau_{12}}{\partial y} + \frac{\partial \tau_{13}}{\partial z}, \quad (19)$$

$$D_v = \frac{\partial \tau_{21}}{\partial x} + \frac{\partial \tau_{22}}{\partial y} + \frac{\partial \tau_{23}}{\partial z}, \quad (20)$$

$$D_w = \frac{\partial \tau_{31}}{\partial x} + \frac{\partial \tau_{32}}{\partial y} + \frac{\partial \tau_{33}}{\partial z}, \quad (21)$$

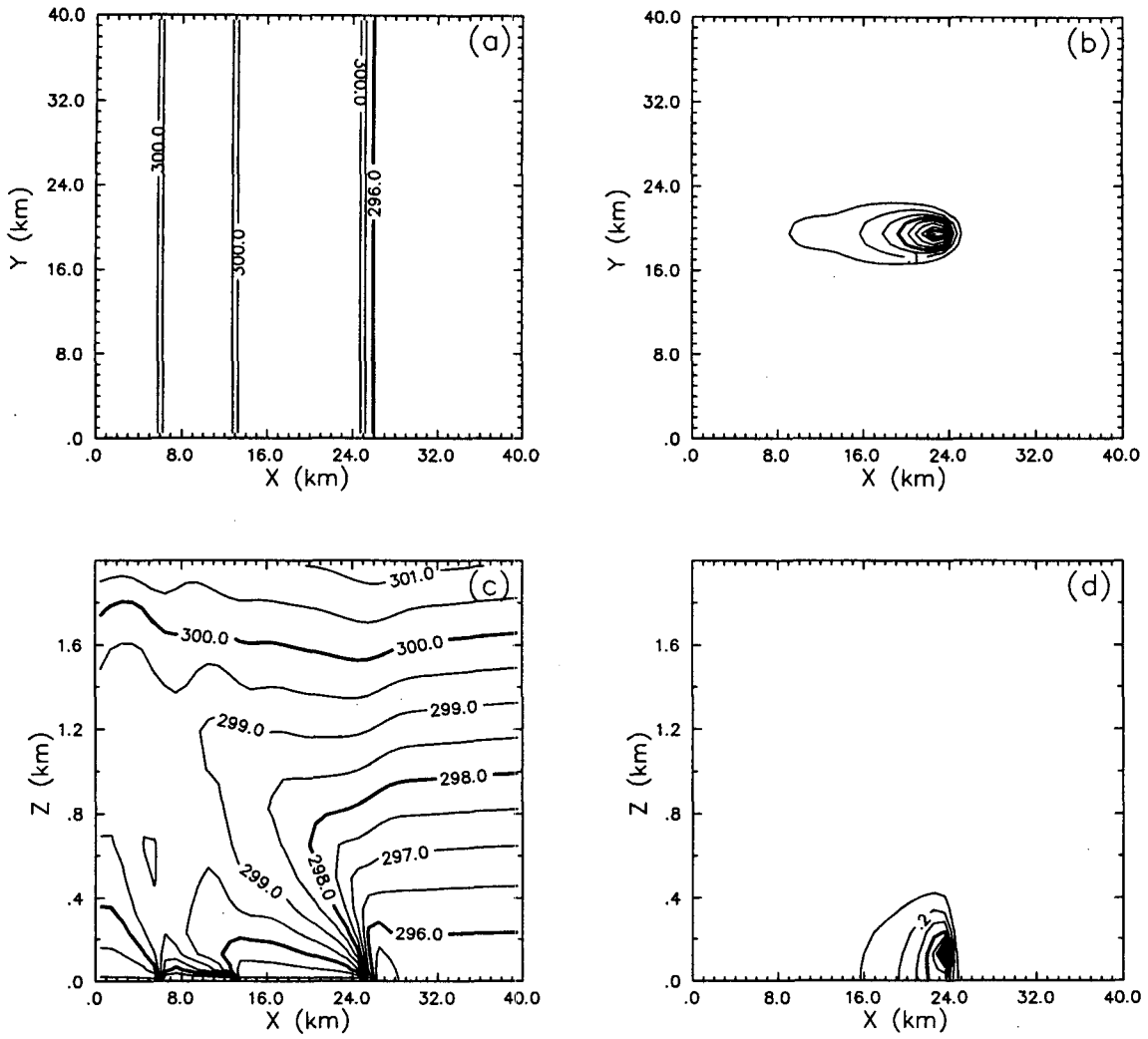

FIG. 5. Simulation over 1D terrain at $t = 1$ h and $N = 0.01$ s^{-1} of (a) potential temperature (K) at the surface; (b) pollutant concentration at the surface, maximum value is 0.453 g m^{-3} and contour interval 0.05 g m^{-3}; (c) x–z section of potential temperature (K); (d) pollutant concentration in x–z section through the continuous point source, maximum contour is 0.919 g m^{-3} and contour interval 0.1 g m^{-3}.

$$\tau_{ij} = K_m\left[D_{ij} - \frac{2}{3}\left(\frac{\partial u}{\partial x} + \frac{\partial v}{\partial y} + \frac{\partial w}{\partial z}\right)\right], \quad (22)$$

$$D_\theta = \frac{\partial}{\partial x}\left(K_h\frac{\partial \theta}{\partial x}\right) + \frac{\partial}{\partial y}\left(K_h\frac{\partial \theta}{\partial y}\right) + \frac{\partial}{\partial z}\left(K_h\frac{\partial \theta}{\partial z}\right), \quad (23)$$

$$D_c = \frac{\partial}{\partial x}\left(K_h\frac{\partial c}{\partial x}\right) + \frac{\partial}{\partial y}\left(K_h\frac{\partial c}{\partial y}\right) + \frac{\partial}{\partial z}\left(K_h\frac{\partial c}{\partial z}\right), \quad (24)$$

where K_m and K_h are the turbulent coefficients for momentum and heat transfer. Here, $K_h/K_m = \text{Pr}$ with Pr representing the Prandtl number.

The key to a turbulence closure scheme is determination of the mixing coefficients. The modified Smagorinsky scheme (Smagorinsky 1963; Lilly 1962) defines K_m as

$$K_m = (k\Delta)^2[\max(|\text{def}|^2 - N^2/\text{Pr}, 0)]^{1/2}, \quad (25)$$

where N is Brunt–Väisälä frequency, k the von Kármán constant, and Δ the minimum grid space. The magnitude of deformation |def| is given by

$$|\text{def}|^2 = \tfrac{1}{2}(D_{11}^2 + D_{22}^2 + D_{33}^2) + D_{12}^2 + D_{13}^2 + D_{23}^2 - \tfrac{2}{3}\,\text{div}^2. \quad (26)$$

Arakawa C grid with a terrain-following coordinate is used in ARPS. A technique that separates the acoustic

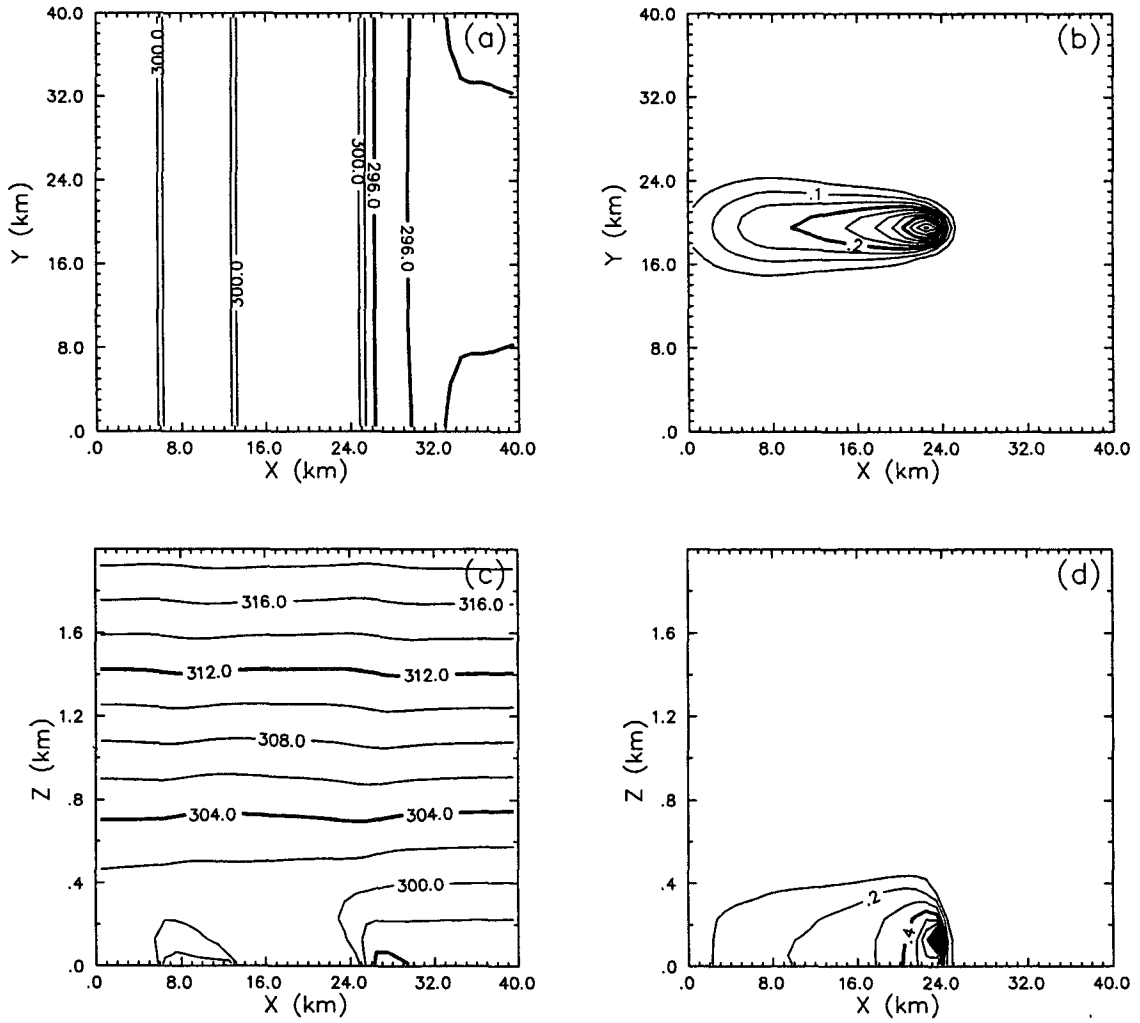

FIG. 6. Simulation over 1D terrain at $t = 1$ h and $N = 0.02$ s^{-1} of (a) potential temperature (K) at the surface; (b) pollutant concentration at the surface, maximum value is 0.563 g m^{-3} and contour interval 0.05 g m^{-3}; (c) x–z section of potential temperature (K); (d) x–z section of pollutant concentration, maximum contour is 1.14 g m^{-3} and contour interval 0.1 g m^{-3}.

waves from other processes is used to solve the fluid dynamics equations. An explicit leapfrog scheme is used with larger time steps for the time integration of the nonacoustic wave terms. The large time step is constrained by the linear stability condition for gravity waves. The forward-in-time scheme is used for the treatment of sound waves. Two options (the explicit and implicit solutions) are given for the time integration of acoustic waves using small time steps. A constraint for the small time steps is required to satisfy the linear stability for sound waves in the explicit solution; however, no constraint for the small time step is needed using the implicit solution. The vertical stretch grid option is used to increase the resolution in the lower layers. Klemp and Wilhelmson (1978) scheme is used for the lateral boundary conditions. The second- and fourth-order computational mixing with constant mixing coefficient are included to filter the computational noise. The Asselin time filter is used to damp the computational mode related to the leapfrog scheme. The divergence damping is used to suppress the acoustic waves. The Rayleigh sponge layer is used to damp the gravity waves that can be reflected back from the top boundary.

The numerical model is initialized using a single sounding. A simple horizontally homogeneous, stratified fluid with a constant Brunt–Väisälä frequency of 0.01 s^{-1} is used as the initial setting for all simulations except in one sensitivity experiment with $N = 0.02$ s^{-1}. Uniform onshore wind of 6.5 m s^{-1} is assumed as the base-state wind in all simulations except one with the calm wind condition. Different from Gaussian dispersions, the pollutant concentration in the numerical model is obtained as the averaged concentration in the

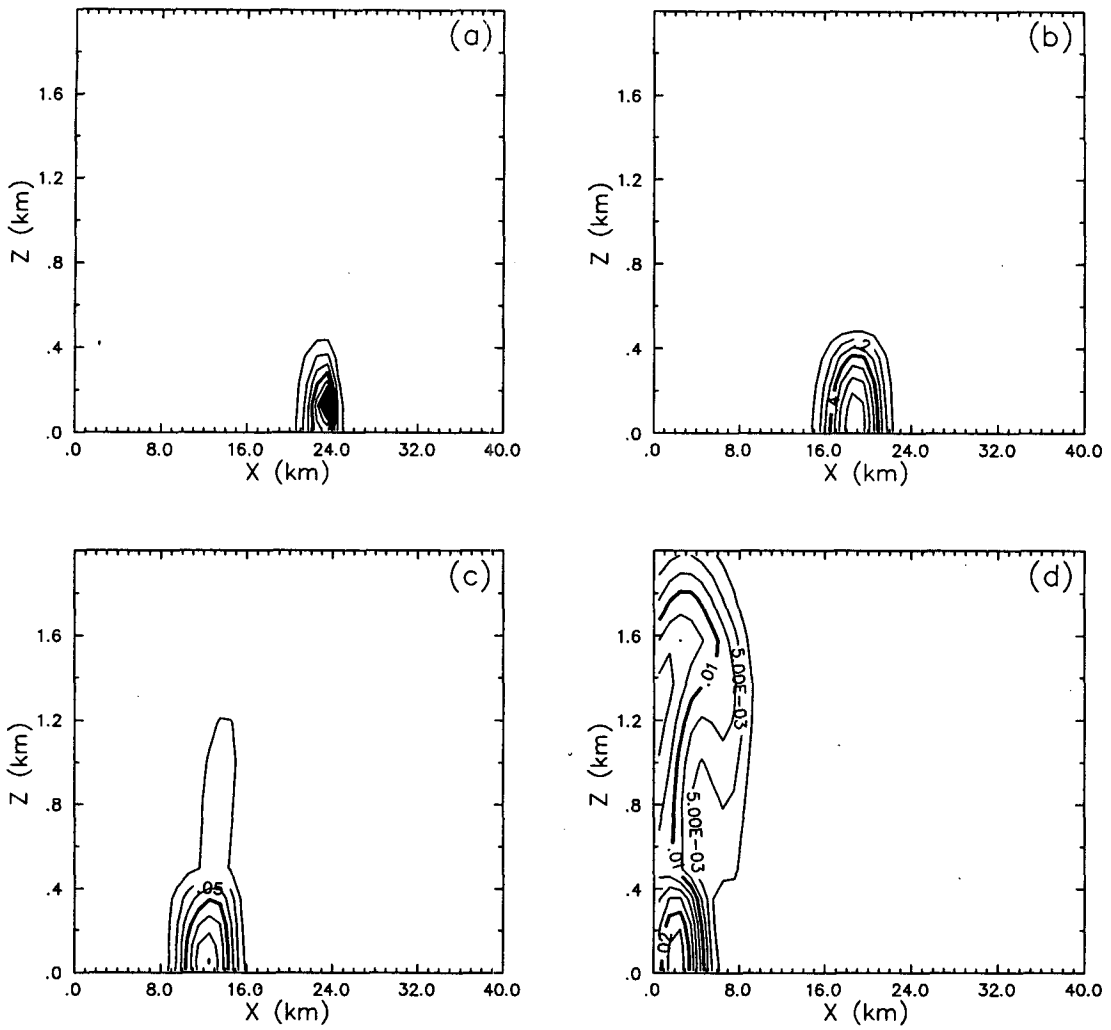

FIG. 7. A sensitivity experiment with a source release time of 5 min. The pollutant concentration (g m^{-3}) in x–z section through the continuous point source with $N = 0.01$ s^{-1} at (a) $t = 300$ s, maximum contour is 11.3 g m^{-3} and contour interval 1.0 g m^{-3}; (b) $t = 600$ s, maximum 0.789 g m^{-3} and contour 0.1 g m^{-3}; (c) $t = 1800$ s, maximum 0.177 g m^{-3} and contour 0.025 g m^{-3}; and (d) $t = 3600$ s, maximum 0.024 g m^{-3} and contour 0.0025 g m^{-3}.

grid volume. Hence, the concentration depends on the model resolution. In most of simulations, the horizontal resolution is 1 km × 1 km. A stretched grid is used in the vertical with an average resolution of 250 m and a resolution of 25 m at the lowest level. The dimensions in the numerical simulations are 41 × 41 × 33. Since the simulations have a high resolution of 25 m in the vertical, the model integration is 0.5 s in order to satisfy the requirement of the linear stability for the gravity waves. Simulation results reach quasi-steady state after 1 h of model integration. One hour is also the approximate time required for the pollutants to be transported from the point source to the western boundary of the domain under an easterly wind. Therefore, an integration time of 1 h is used for this study. The release time is the same as the integration time for the continuous source except in one sensitivity experiment where a release time of only 5 min is assumed to simulate a finite source with the same amount of material. Radiating boundary conditions are used at the boundaries.

b. Comparison with the Gaussian dispersion

To compare with the Gaussian dispersion, a numerical simulation, considered as a control run experiment, is designed here with 1D terrain distribution, a straight coastline, and a straight Indian River. This simulation has the same kind of ocean–land–river pattern as that in the Gaussian dispersion and also has the same surface temperature distribution (Fig. 5a). The meteorological background is similar: the onshore inflow has a

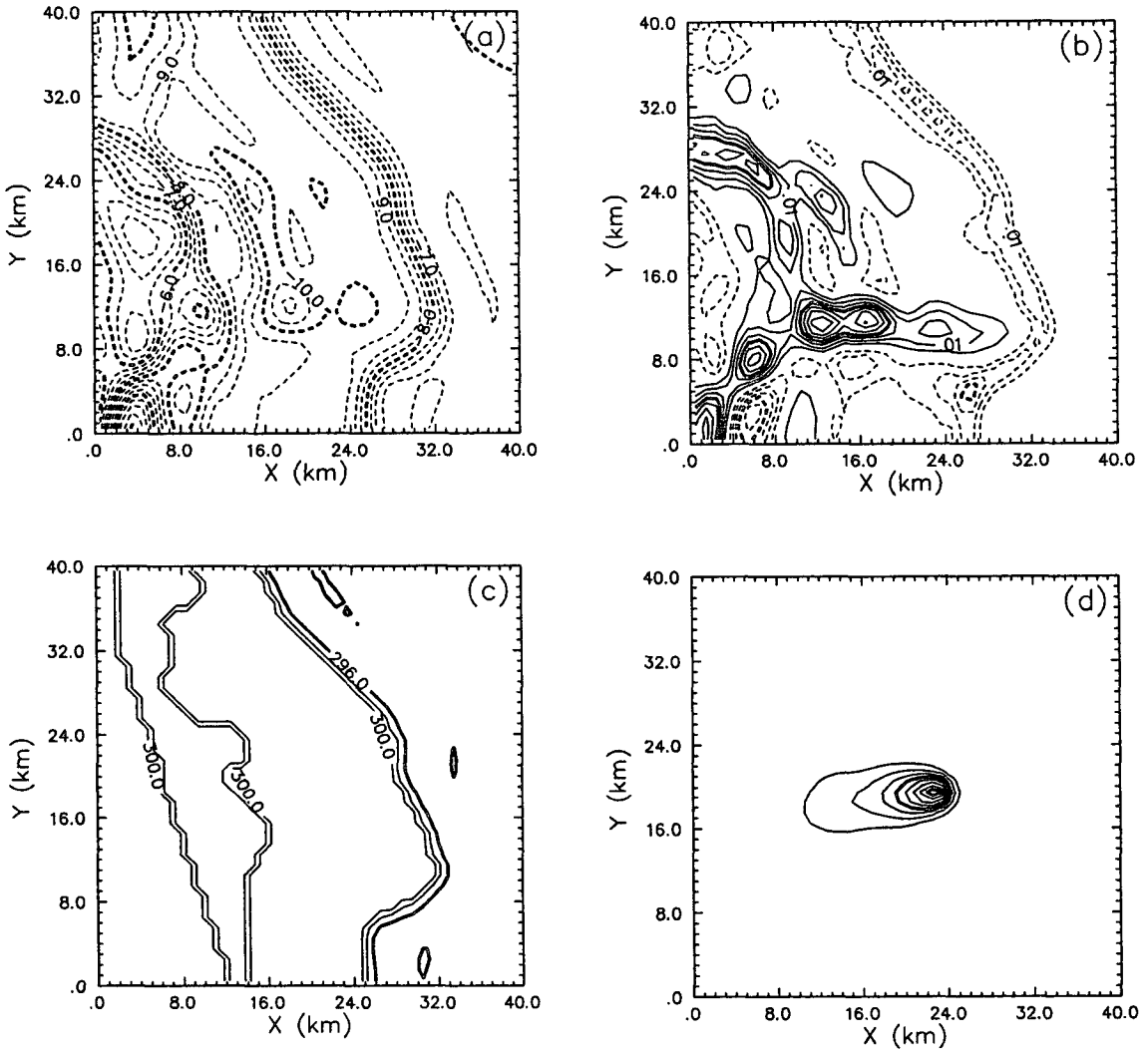

FIG. 8. Surface distribution in real terrain simulation at $t = 1$ h and $N = 0.01$ s^{-1} of (a) u (m s^{-1}), maximum easterly wind is 12.1 m s^{-1} and contour interval 0.5 m s^{-1}; (b) w (m s^{-1}), maximum value 0.04 m s^{-1} and contour 0.005 m s^{-1}; (c) potential temperature (K); and (d) pollutant concentration (g m^{-3}), maximum value 0.442 g m^{-3} and contour 0.05 g m^{-3}.

wind speed of 6.5 m s^{-1} and a Brunt–Väisälä frequency of 0.01 s^{-1} for stability. A major difference between the Gaussian dispersion and the Eulerian dispersion are that Gaussian model has a constant diffusivity and does not consider local circulations. When the local circulations are not strong, the basic TIBL structure is determined by the surface temperature difference, upwind speed, and inflow stability. The TIBLs can still be retrieved in the 3D simulation. Because the Gaussian dispersion is a steady-state solution, it is imperative that the quasi-steady-state numerical simulation is used to compare with it.

After 1 h of integration, the model reaches a steady state. Figure 5c shows a vertical structure of the TIBL through the potential temperature field. Parabolic shape of the temperature contour indicates the shape of the TIBL. Two convective TIBLs forms over land and one stable shallow TIBL forms over the river. The numerical simulation shows a similar structure of the TIBLs as that predicted by Eq. (6). The TIBL near the shoreline reaches about 900 m at 10 km downwind of the coastal line and is about 50% higher than the TIBL 1 in Fig. 2. This increase might have been caused by the upward branch of the sea-breeze circulation. The TIBL height above the Indian River (TIBL 2) is about 200 m, same as the one predicated by Eq. (6). The TIBL caused by the river–land interface is 700 m at western boundary, about 10% lower than TIBL 3. This is due to the fact that Eq. (6) is not appropriate for near-neutral condition. The numerical simulations produce a pattern with one TIBL existing within another when a stratified onshore flow passes over complex topogra-

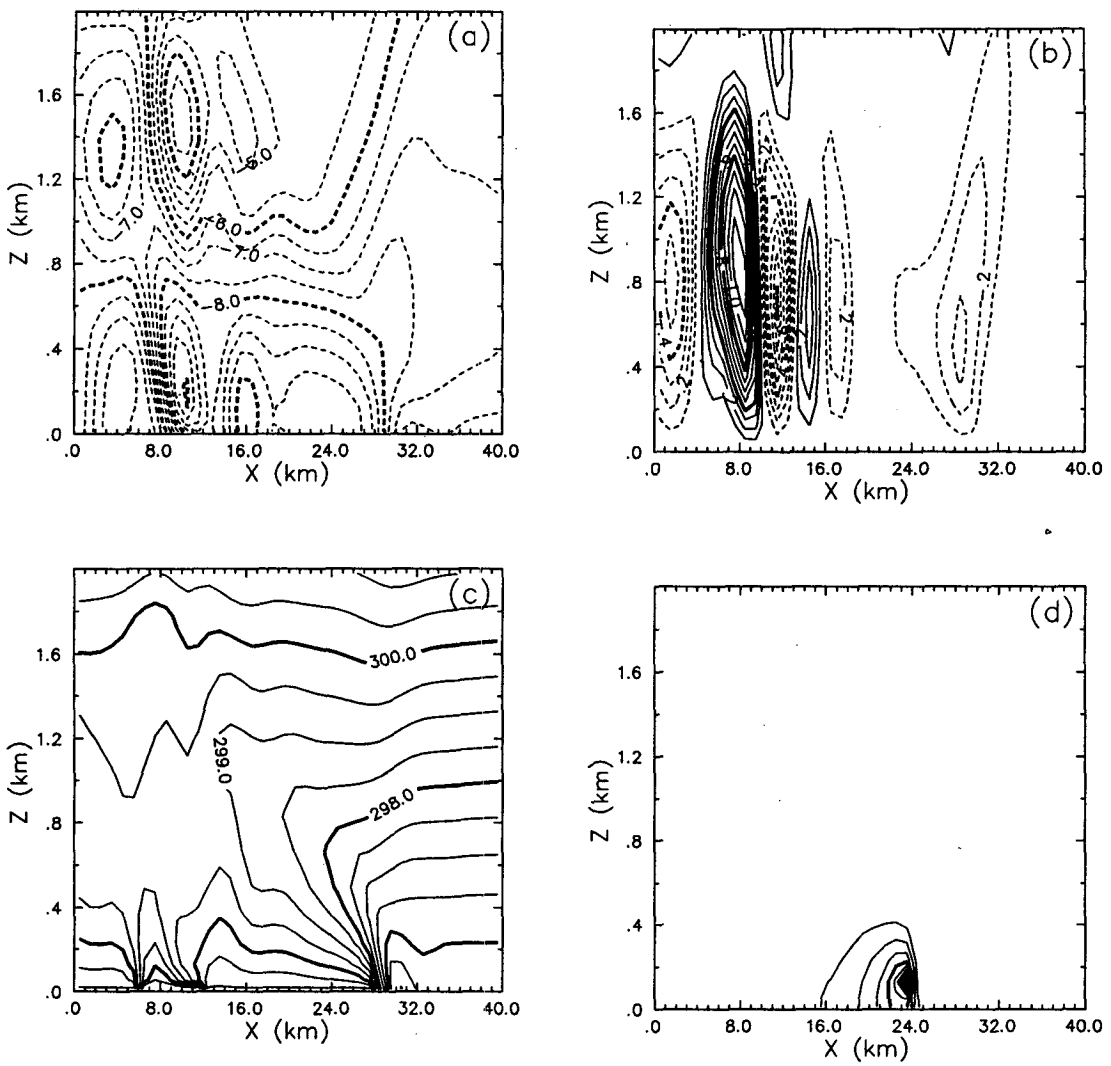

FIG. 9. The x–z section through the continuous point source in real terrain simulation at $t = 1$ h and $N = 0.01$ s^{-1} of (a) u (m s^{-1}), maximum easterly wind is 10.3 m s^{-1} and contour interval 0.5 m s^{-1}; (b) w (m s^{-1}), maximum value 1.15 m s^{-1} and contour 0.1 m s^{-1}; (c) potential temperature (K); and (d) pollutant concentration (g m^{-3}), maximum value 0.958 g m^{-3} and contour 0.1 g m^{-3}.

phy. These results support the TIBL within TIBL structure shown in Fig. 2.

Three local circulations form and are caused by three interfaces between ocean, land, and river. The circulations appear to increase the low-level wind speed by about 30% over the land surface and decrease by about 30% over the river. Since the ocean–land breeze increases the wind speed at low levels, the pollutants are transported more quickly downwind. This local circulation also extends the plume in the vertical direction. The maximum ground level concentration of 0.453 $\times 10^6$ μg m^{-3} (Fig. 5b) is much smaller than the Gaussian estimation. This reduction is mostly due to the use of a grid volume averaged concentration in the numerical simulations. The plume here is about 7.5 km in width according to the 2×10^4 μg m^{-3} contour line. This corresponds to an increase of about 50% in the width of the Gaussian plume. However, it is shorter than the Gaussian plume because the circulations caused by the temperature contrast between the land and river decreases the wind speed over the river and hence suppresses the transport downwind. The circulations disperse the pollutants in the vertical and the low concentration is found at the top of the TIBL. The maximum concentration in the whole domain is 0.919 $\times 10^6$ μg m^{-3}, as can be seen in a vertical section through the point source (Fig. 5d). This value is two times as large as the maximum ground level concentration, which indicates that the pollutants are not fully mixed in the vertical as was found in the Gaussian dis-

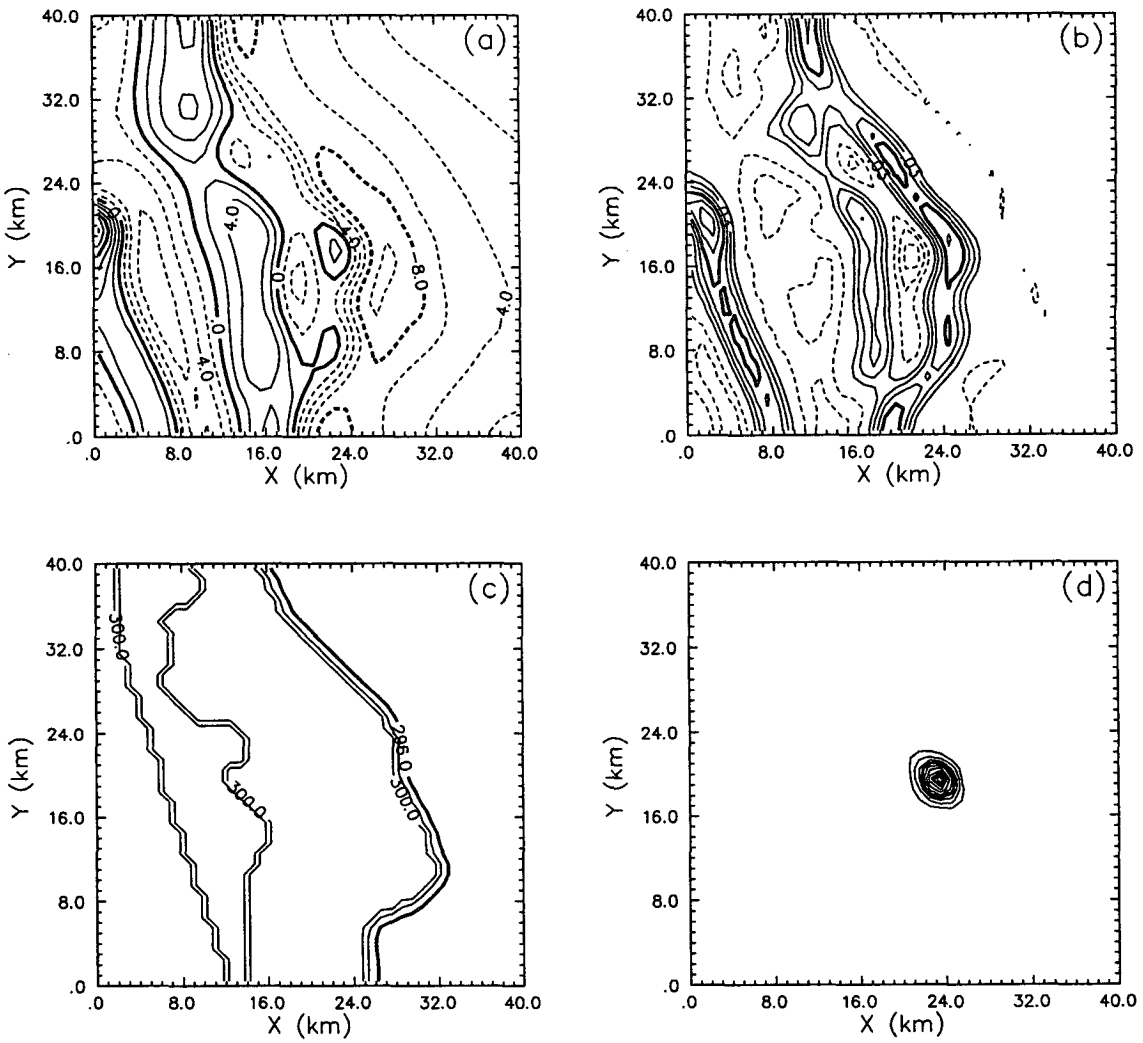

FIG. 10. Surface distribution in real terrain simulation at t = 1 h and N = 0.01 s^{-1} with no initial ambient wind for (a) u (m s^{-1}), maximum easterly wind is 12.3 m s^{-1} and contour interval 2.0 m s^{-1}; (b) w (m s^{-1}), maximum value is 0.08 m s^{-1} and minimum −0.043 m s^{-1}; (c) potential temperature (K); and (d) pollutant concentration (g m^{-3}), maximum value is 0.503 g m^{-3} and contour 0.05 g m^{-3}.

persion. The maximum concentration in the Gaussian dispersion is four times larger than that in the numerical simulation. If the Gaussian concentration field is converted to grid-averaged concentration by using nine-point smoothing, the maximum of the averaged concentration is 1.102×10^6 μg m^{-3}. The difference in concentration is now less than 20%. Similar dispersion patterns of the plume and the same order of magnitude of the maximum concentration show that the results from the Gaussian dispersion model and the Eulerian dispersion model are similar.

c. *Numerical sensitivity experiments*

Several numerical sensitivity experiments are conducted to investigate the effects of stability, release time, rate of release, topography, and the calm wind condition where the vertical wind shear caused by the local circulations dominates and Gaussian dispersion equation is unsuitable. All the numerical simulations here include effects of local circulations and the TIBLs caused by the ocean–land–river–land interaction. The numerical results also show that the concentration is very sensitive to the model resolution. The reduction in horizontal resolution affects the concentration distribution much more than the reduction in vertical resolution.

1) SENSITIVITY TO DIFFERENT UPWIND STRATIFICATION

Upwind atmospheric stability is important since it affects TIBL formation, which in turn influences the

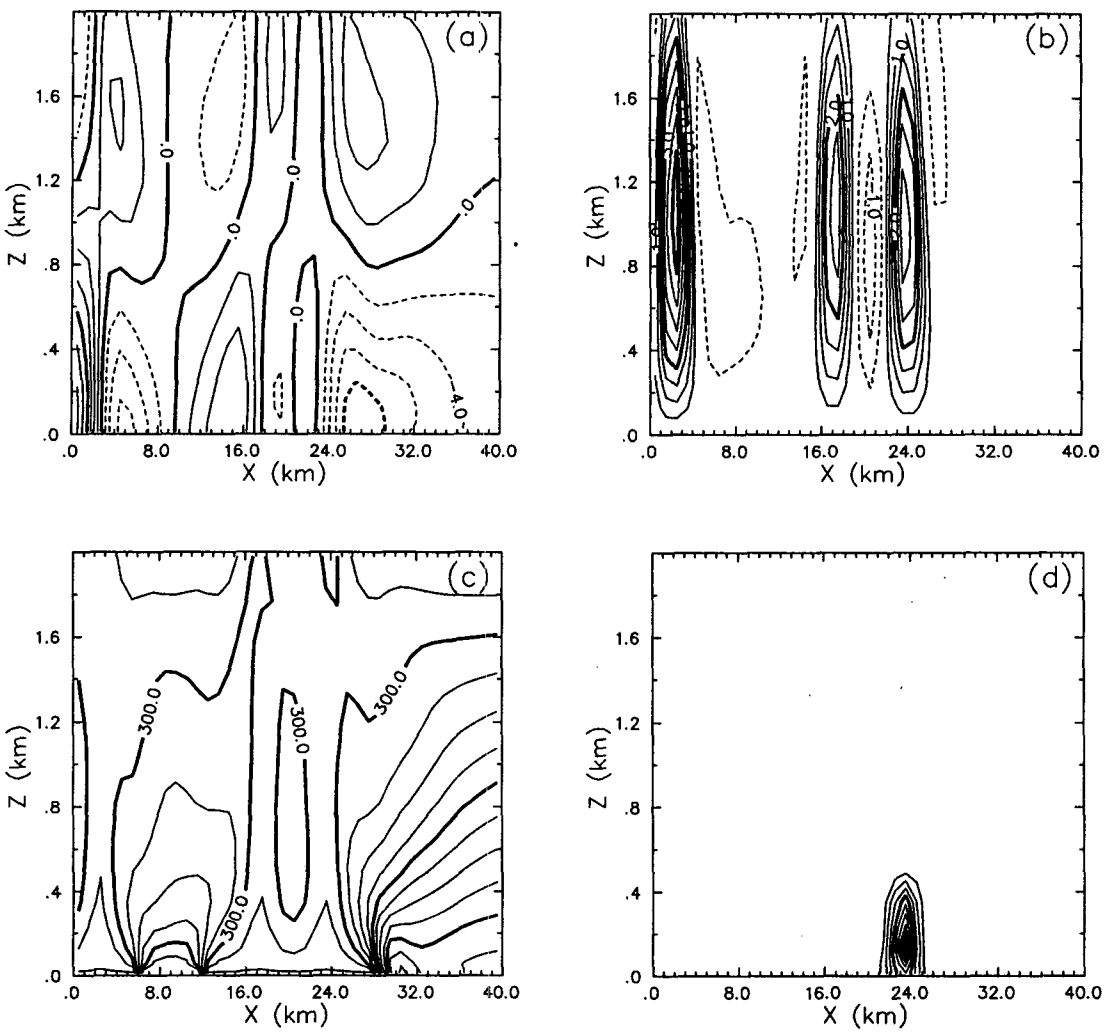

FIG. 11. The $x-z$ section through the continuous point source in real terrain simulation at $t = 1$ h and $N = 0.01$ s^{-1} with no initial ambient wind for (a) u (m s^{-1}), maximum easterly wind is 12.5 m s^{-1} and contour interval 2.0 m s^{-1}; (b) w (m s^{-1}), maximum value 4.4 m s^{-1} and contour 0.5 m s^{-1}; (c) potential temperature (K); and (d) pollutant concentration (g m^{-3}), maximum value 1.24 g m^{-3} and contour 0.1 g m^{-3}.

dispersion characteristics. When the onshore flow is very stable, the TIBL height is shallow and the volume over which pollutants diffuse is smaller. The sensitivity experiment here is the same as the control run except that $N = 0.02$ s^{-1}. It has the same surface temperature distribution (Fig. 6a), but the vertical potential temperature gradient is four times that in the control run (Fig. 6c). The predicted TIBL height in this case is about 400 m at 10 km from the point source, about half the TIBL height in the control case. This result supports the relation between the stability γ and the TIBL height in Eq. (6). Local circulations are depressed in both the u and w fields as compared to the control run case. Pollutants are mostly found below 400 m, trapped within the TIBL (Fig. 6d). The plume is wider (about 11 km) and thicker in downwind direction since much more pollutants are transported there and the diffusion is low (Figs. 6b,d). For example, the surface concentration at 10 km from the elevated point source is 0.25 $\times 10^6$ μg m^{-3}, about three times the concentration in the control run. Since the local circulation is weaker, its effect is not obvious in the concentration distribution. The maximum surface concentration is 0.563 $\times 10^6$ μg m^{-3}, and the maximum concentration in the whole domain is 1.14 $\times 10^6$ μg m^{-3}, both showing an increase of about 24% as compared to those in the control run.

2) EFFECT OF RELEASE PERIOD

Dispersion from a finite source is different from the dispersion from a continuous source. An experiment

with 5-min release from the elevated point source with the same total release is designed here to investigate the differences in the dispersion patterns. To keep the same total release, the actual release rate for 5 min has to be 12 times as large. The meteorological parameters are the same as in the control run.

Most of the pollutants are located near the elevated point source at the time (t = 300 s) when the source stops releasing the material (Fig. 7a). During the release time the pollutants are not transported much downwind. The maximum concentration is 11.3×10^6 $\mu g\ m^{-3}$ at this time and is almost 13 times larger than that of the control run. This period of dispersion is still like a continuous release. After that time (the first 5 min), there is no pollutant release and the material is transported downwind like a puff. At t = 900 s, the puff becomes larger and moves away from the point source mostly transported by the ambient onshore wind (Fig. 7b). At the top of the puff, effect of the local circulation can be seen. The pollutants decay very fast and have a maximum value of 0.789×10^6 $\mu g\ m^{-3}$, about 14% less than that in control run. The puff moves farther to the west, and the maximum concentration is 0.177×10^6 $\mu g\ m^{-3}$ at 30 min (Fig. 7c). At 1 h, the puff is at the western boundary of the model domain and is very weak with a maximum concentration of 0.24×10^5 $\mu g\ m^{-3}$ (Fig. 7d). Results thus show that the release time plays a major role in the dispersion pattern.

3) Effect of real terrain distribution

The topography of the Cape Canaveral coastline in Florida, including the shape of the Indian River and the coastline orientation, is considered in this simulation. The purpose of this simulation is to investigate the effects of the real topography. All other conditions are similar to those in the control run.

Figure 8c shows a sudden change in potential temperature along the Cape Canaveral coastline and around the Indian River. Unlike the setting in the control run, variations of the surface temperature in the y direction are considered. Acceleration of the onshore wind is predicted over the land and deceleration over the Indian River (Fig. 8a). The local circulations are more complex (Fig. 8b). A convergence zone occurs near the coastline and a divergence zone above the Indian River. The pollutant plume becomes wider (8 km) and shorter above the divergence zone. The maximum ground-level concentration is 0.442×10^6 $\mu g\ m^{-3}$, close to the value in the control run (Fig. 8d).

The structure of the mesoscale circulations is shown through a vertical section across KSC (Figs. 9a,b). The overall TIBL pattern represented by the potential temperature field is very similar to that in the control run (Fig. 9c). The sea–land breeze circulation is similar to that in the control run, but the local river–land circulations are stronger (Fig. 9d). The pollutants are not advected farther downwind and the plume is shorter. Most of the pollutants are trapped below 400 m in the vertical. The dispersion pattern outlined by the 0.02×10^6 $\mu g\ m^{-3}$ contour is also similar to that in the control run. The maximum concentration is 0.958×10^6 $\mu g\ m^{-3}$, 1.04% of that in the control run simulation. These numerical experiments indicate that the control run without the real topography can be used to represent the general dispersion pattern. However, local differences in concentrations are caused by the shape of the Indian River and the coastline.

4) Dispersion in calm initial wind

The dispersion pattern in calm wind conditions could be very different from that with initial ambient wind. To investigate this phenomenon, the sensitivity experiment is conducted with the same topography (Fig. 10c), but with no ambient wind. In this case, Gaussian dispersion models become invalid because of strong circulations. The slender-plume approximation is no longer valid under these conditions.

Surface potential temperature is set the same as the previous case with the land warmer than the ocean and the river (Fig. 10c). Under this kind of surface forcing, sea and river breezes dominate (Fig. 10a). Surface convergence lines associated with the heated land and a surface divergence line associated with the cool river surface can be seen. The convergence zones correspond with upward motion, while the divergence zones correspond with the downward motion (Fig. 10b). Surface flow is more complicated and the pollutants are mostly located near the source, which is totally different from the dispersion with ambient wind (Fig. 10d). Strong local circulations prevent the pollutants from being transported away from the source. The maximum ground-level concentration is 0.503×10^6 $\mu g\ m^{-3}$, larger than that in the previous case with ambient wind.

The ocean–land and river–land circulations, driven by the local surface temperature differences, are shown in Fig. 11a. These three circulations are especially seen clearly in the vertical cross section of the w field (Fig. 11b). The maximum vertical velocity reaches 4.4 $m\ s^{-1}$, as against 1.2 $m\ s^{-1}$ for the case with an initial ambient wind. The TIBL within TIBL structure in the previous case is not seen, and strong circulations help the surface effects to be extended to higher levels (Fig. 11c). Because of the strong local circulations associated with the sea-breeze front, most of the pollutants are located near the source with no downwind transport (Fig. 11d). Some of the pollutants are transferred to higher levels. Domain maximum concentration reaches 1.24×10^6 $\mu g\ m^{-3}$, increasing by 29.4% as compared to that with uniform wind upstream. This sensitivity experiment shows that the local circulations are stronger for calm ambient wind, and they do play an important role in the dispersion.

4. Summary

Dispersion from an elevated release near the Florida coastline has been estimated using two different models. One is a Gaussian dispersion model, and the other is an Eulerian dispersion model coupled with a nonhydrostatic meteorological model. The temperature difference between land and ocean generates a local sea–land circulation. A thermal internal boundary layer (TIBL) also develops. Both play a significant role in the coastal dispersion.

The Gaussian model is generally used in simple meteorological conditions. A modified Gaussian model that includes the effect of TIBL is normally used in the coastal region. Results show that the concentrations obtained from these two distinctly different methods are the same order of magnitude and the plumes have similar dispersion patterns. However, Gaussian dispersion does not provided detailed structure of the plume. One shortcoming of the numerical simulation is that the concentrations are grid averaged. Sensitivity experiments with the numerical model reveal that the coastal dispersion is affected by magnitude of the ambient wind, upwind stability, source release time, grid resolution, and coastal topography.

Acknowledgments. The authors wish to thank CAPS for making the ARPS model available. We would like to thank Dr. Ming Xue for several helpful suggestions on using the ARPS model and Dr. William Bauman for providing the information on the source data. We would like to thank anonymous reviewers who helped to improve the quality of this paper. The numerical simulations were performed using the Facilities for Ocean/Atmospheric Modeling and Visualization (FOAMv) of North Carolina State University and the North Carolina Supercomputing Center, RTP. This study was supported by the Atmospheric Science Division, National Science Foundation under Grant ATM-92-12636.

REFERENCES

Boybeyi, Z., and S. Raman, 1992: A three-dimensional numerical sensitivity study of convection over the Florida peninsula. *Bound.-Layer Meteor.,* **60,** 325–359.

Briggs, G. A., 1973: Diffusion estimation for small emission. 1973 Annual Report, Air Resources Atmos. Turb. and Diffusion Lab., Environmental Res. Lab., Report ATDL-106, USDOC-NOAA, 59 pp.

CAPS, 1993: ARPS Version 3.1 User's Guide. Center for Analysis and Prediction of Storms, University of Oklahoma, 183 pp.

Deardorff, J. W., and G. W. Willis, 1982: Ground-level concentrations due to fumigation into an entraining mixed layer. *Atmos. Environ.,* **16,** 1159–1170.

Klemp, J. B., and R. B. Wilhelmson, 1978: The simulation of the three-dimensional convective storm dynamics. *J. Atmos. Sci.,* **35,** 1070–1096.

Lilly, D. K., 1962: On the numerical simulation of buoyant convection. *Tellus,* **14,** 168–172.

Misra, P. K., 1980: Dispersion from tall stacks into shore line environment. *Atmos. Environ,* **14,** 393–397.

Plate, E. J., 1971: Aerodynamic characteristics of atmospheric boundary layers. U.S. Atomic Energy Commission TID-25465, 190 pp.

Raman, S., 1982: Observations of the boundary layer wind structure near the land–sea interface, Preprints, *First Int. Conf. on Meteorology and Air–Sea Interaction of the Coastal Zone,* The Hague, the Netherlands, Amer. Meteor. Soc., 4–7.

Raynor, G. S., P. Michael, R. M. Brown, and S. Raman, 1975: Studies of atmospheric diffusion from a near shore oceanic site. *J. App. Meteor.,* **14,** 1080–1094.

Smagorinsky, J., 1963: General circulation experiments with the primitive equations. *Mon. Wea. Rev.,* **91,** 99–164.

Turner, D. B., 1994: *Workbook of Atmospheric Dispersion Estimates.* Luwis, 166 pp.

Uliasz, M., 1993: The atmospheric mesoscale dispersion modeling system. *J. Appl. Meteor.,* **32,** 139–149.

van Dop, H., R. Steenkist, and F. T. M. Nieuwstadt, 1979: Revised estimates for continuous shoreline fumigation. *J. Appl. Meteor.,* **18,** 133–137.

Venkatram, A., 1977: A model of internal boundary-layer development. *Bound.-Layer Meteor.,* **11,** 419–437.

——, 1988: Topics in applied dispersion modeling. *Lectures on Air Pollution Modeling,* A. Venkatram and J. C. Wyngaard, Eds., Amer. Meteor. Soc., 267–324.

Weisman, B., 1976: On the criteria for the occurrence of fumigation inland from a large lake—A reply. *Atmos. Environ.,* **12,** 172–173.

Yamada, T., S. Bunker, and M. Moss, 1992: Numerical simulation of atmospheric transport and diffusion over coastal complex terrain. *J. Appl. Meteor.,* **31,** 565–578.